http://dx.doi.org/10.21577/0100-4042.20170634 *Quim. Nova,* Vol. 44, No. 1, 98-104, 2021

Nota Técnica

PREPARATION AND PROPERTIES OF PT-RH-PD / CEO_2-ZRO_2-LA_2O_3-AL_2O_3 FIBROUS CATALYST VIA ELECTROSPINNING

Yu Zhu[a], Wei-gang Shen[a,*], Shuai-shuai Lv[a], Hong-jun Ni[a] and Xing-xing Wang[a]
[a]School of Mechanical Engineering, Nantong University, 226019 Jiangsu – Nantong, China

Recebido em 06/04/2020; aceito em 14/07/2020; publicado na web em 10/09/2020

In order to increase the specific surface area of Pt-Rh-Pd / Al_2O_3 automotive three-way catalyst and improve its low-temperature reduction performance, Ce, Zr, and La were added to the Pt-Rh-Pd / Al_2O_3 catalyst to prepare the fibrous Pt-Rh-Pd / CeO_2-ZrO_2-La_2O_3-Al_2O_3 catalyst via an electrospinning technique. The fibrous catalysts were characterized by XRD, FT-IR, SEM-EDS, H_2-TPR and BET analysis. The catalytic effect of the catalyst on automobile exhaust was also studied. Results revealed that the surface of catalysts is mainly mesoporous. Ce, Zr and La can remarkably increase the specific surface area of the Pt-Rh-Pd / Al_2O_3 catalyst. The specific surface area of the catalyst prepared with Pt Rh Pd molar ratio of 0.75:0.01:1 is 301.5816 $m^2\ g^{-1}$, and the average diameter of which is 790 nm. In addition, the reaction temperature of the catalyst is approximately 220 °C, which shows good low-temperature reduction performance. Moreover, the Pt-Rh-Pd / CeO_2-ZrO_2-La_2O_3-Al_2O_3 catalyst has a catalytic conversion efficiency for NO_X of 90.0% in automobile exhaust, a catalytic conversion efficiency for CO of 88.8%, and a catalytic conversion efficiency for SO_2 of 75%.

Keywords: electrospinning; fiber; three-way catalyst; composite metal oxide; rare earth element.

INTRODUCTION

With the rapid growth of the number of automobiles in the world, hydrocarbons (HC), carbon monoxide (CO) and nitrogen oxides (NO_X) in automobile exhausts have increasingly polluted the air of cities.[1-3] Automotive exhaust purification catalyst is essential for controlling exhaust pollution.[4,5] Automobile exhaust purification catalyst carrier is generally composed of rare earth oxygen storage material and Al_2O_3 with high specific surface area, strong heat resistance and aging resistance.[6-11] As is well known, high-performance rare earth oxygen storage material is a key component of automobile exhaust purification catalyst,[12-14] which determines the catalytic performance and life of catalyst. As a consequence, improving the oxygen storage performance, specific surface area and thermal stability of the carrier are the main directions for the development of high-performance automotive exhaust purification catalyst.

Since the 1980s, CeO_2-ZrO_2-Al_2O_3 carrier has shown excellent oxygen storage performance in automotive exhaust purification catalyst.[15] CeO_2-ZrO_2-Al_2O_3 carrier remarkably improves the dispersion of active components on the surface of the carrier and catalytic activity.[16,17] In addition, CeO_2-ZrO_2-Al_2O_3 carrier can enhance the anti-poisoning ability of automobile exhaust evolution catalysts.[18] It is beneficial to promote the water vapor conversion and steam reforming reactions and improve the catalytic conversion efficiency of the catalyst.[19] However, CeO_2-ZrO_2-Al_2O_3 carrier is easy to sinter at high temperature, which causes its specific surface area to drop sharply and results in a significant decrease in its oxygen storage / release performance. Moreover, CeO_2-ZrO_2-Al_2O_3 carrier cannot fully adapt to the high temperature working state of automobile exhaust purification catalyst. It was found that the incorporation of Pr, Y, Nd plasma could obviously promote the high temperature stability of CeO_2-ZrO_2-Al_2O_3 support and strengthen the sintering resistance of the catalyst.[20] The performance of the carrier affects not only the dispersion of precious metals, but also the high temperature stability of the catalyst.[21] Therefore, the preparation of carrier with high temperature stability and high oxygen storage capacity has become one of the important means to improve the catalytic effect of three-way catalysts. The precious metals such as Pt, Pd and Rh are the mainly active components of the three-way catalyst.[22] Reducing the amount of precious metals while enhancing the low-temperature catalytic activity and high-temperature thermal stability of the catalyst are the main goals of the catalyst development. In recent years, electrospinning technology can easily and effectively prepare nano to sub-micron fibers, which has been widely applied in catalyst research.[23-25] The polymer prepared by electrospinning has a relatively controllable chemical environment and structure on the surface, which can be used to prepare nanoparticle catalysts with extremely high dispersion and large specific surface area.[26] The fiber catalyst prepared via electrospinning can effectively solve the problems of difficult aggregation, shedding and deactivation of catalytically active particles.[27] The impregnation method is a common method for preparing automobile exhaust purification catalysts. However, the catalyst prepared by the impregnation method exists problems of poor catalytic performance at low temperature and metal particles' sintering at high temperature, which seriously diminishes the catalytic activity and shortens the life of catalysts.

In this study, Ce, Zr, and La were added to the Pt-Rh-Pd / Al_2O_3 catalyst to prepare the fibrous Pt-Rh-Pd / CeO_2-ZrO_2-La_2O_3-Al_2O_3 catalyst via an electrospinning technique. The fibrous catalysts were characterized by XRD, FT-IR, SEM-EDS, H_2-TPR and BET analysis to study their microstructural and compositional evolution. This work provides a simple route to improve the catalytic performance for CO and NO_X in automobile exhaust.

EXPERIMENT

$AlCl_3$, $ZrCl_4$, $CeCl_4$ and $LaCl_3$ were dissolved in the mixed solution of 30 mL CH_2Cl_2 and 0.95 mL $C_6H_{14}O$ with the Ce Zr La and Al molar ratio of 1:1:0.06:2, while the mass fraction of $AlCl_3$ is 1.94 wt.%. The solution was subsequently dried at 80 °C for 2 h to obtain white powder named $CeCl_4$-$ZrCl_4$-$LaCl_3$-$AlCl_3$. The white powder, as well as PVP, were then dissolved in the mixed solvent of 9 mL C_2H_5OH and 4 mL DMF, in which the content of mass fraction was 4 wt.%. Finally, Pt Rh and Pd molar ratios of

*e-mail: swg13962801659@163.com

Figure 1. *Process scheme of preparing Pt-Rh-Pd / CeO_2-ZrO_2-La_2O_3-Al_2O_3 fibrous catalysts by electrospinning*

0.75:0.01:1, 0.75:0.23:1 and 0.75:0.34:1 were respectively dissolved in the mixed solution to prepare Pt-Rh-Pd / CeO_2-ZrO_2-La_2O_3-Al_2O_3 precursor solution. The precursor solution of Pt-Rh-Pd / CeO_2-ZrO_2-La_2O_3-Al_2O_3 was loaded by a 10 mL syringe with a stainless-steel needle whose diameter was 0.8 mm. Several parameters related to electrospinning are listed in Table 1. Process scheme of preparing Pt-Rh-Pd / CeO_2-ZrO_2-La_2O_3-Al_2O_3 fibrous catalyst by electrospinning is showed in Figure 1.

Table 1. Electrospinning parameters

Parameters	Value
Spinning voltage	17 ± 0.5 (kV)
Spinning distance	17 ± 0.5 (cm)
Advancing speed	0.003 ± 0.0005 (mm s^{-1})

X-ray diffraction (XRD) patterns were collected using a Rigaku DX-2500 diffractometer with Cu Kα radiation (0.15406 nm) in the range of 10°-90° with a step size of 0.02°. Fourier transform infrared spectrometer (FT-IR) patterns were measured employing a Vertex 70 Fourier infrared spectrometer. The BET specific surface area (Brunauer Emmett Teller, BET) for determining the specific surface area, catalyst pore volume, catalyst pore size and distribution of the catalyst were tested employing ASAP 2020 specific surface area and mesoporous / microporous analyzer. Scanning Electron Microscope (SEM) images were observed applying a Hitachi HITA CHI S-3400N scanning electron microscope. H_2 temperature-programmed reduction (H_2-TPR) studies were carried out using a Chem-Star program temperature reduction instrument to observe the reduction characteristics of the catalysts. Prior to the experiment, the sample was pretreated in N_2 (25 mL min^{-1}) at 450 °C for 1 h.

The catalytic activity of Pt-Rh-Pd / CeO_2-ZrO_2-La_2O_3-Al_2O_3 fibrous catalyst was evaluated in a Dong feng LZ6430BQBE car with a self-assembled catalytic device. As displayed in Figure 2, Pt-Rh-Pd / CeO_2-ZrO_2-La_2O_3-Al_2O_3 fibrous catalyst was wrapped on the surface of ceramic rods and fixed in the self-assembled catalytic device with metal mashes. The smoke and dust samplers were used to collect automobile exhaust. Both a portable infrared CO analyzer and a gas chromatography mass spectrometer were used to detect the components and contents of the exhaust. The catalytic conversion efficiency was calculated by the following formula in which A represented contaminant content before catalyst installation and B represent contaminant content after catalyst installation.

$$\text{Catalytic conversion} = \frac{A-B}{A} \times 100\% \quad (1)$$

RESULTS AND DISCUSSION

Composition and structure of Pt-Rh-Pd / CeO_2-ZrO_2-La_2O_3-Al_2O_3 fibrous catalyst

Figure 3 presents the XRD spectrum of a Pt-Rh-Pd / CeO_2-ZrO_2-La_2O_3-Al_2O_3 fibrous catalyst. From Figure 3, It can be found that characteristic diffraction peaks corresponding to the Al_2O_3 crystal structure appear at 2θ of 41.28°, 47.49°, 68.78° and 83.32°. The diffraction peak width is narrow, and the peak value is high, which indicate that the crystallization of Al_2O_3 crystals is excellent. Characteristic diffraction peaks with 2θ of 24.58°, 32.45°, 48.62°, 48.70°, 57.64° and 62.15° correspond respectively to the crystal planes of (111), (200), (220), (311), (222) and (400) cubic phases appearing on the spectrum, which are consistent with the CeO_2-ZrO_2 solid solution fluorite structure. The peak at 2θ of 52.45° reveals that the catalyst has a small amount of La_2O_3 crystal structure. CeO_2-ZrO_2-La_2O_3 not only plays the role of oxygen storage, but Zr^{4+} in CeO_2-ZrO_2-La_2O_3 also improves the dispersion among the catalyst carrier particles and the thermal stability of the active components, thus ensuring the catalytic performance.[20] The presence of CeO_2 and La_2O_3 can occupy the active sites on the support surface and inhibit

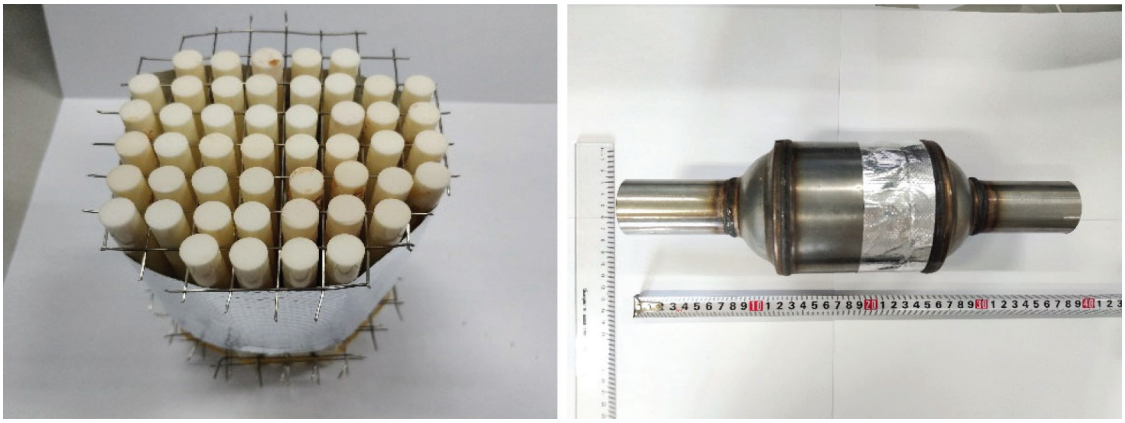

Figure 2. *Catalytic device diagram*

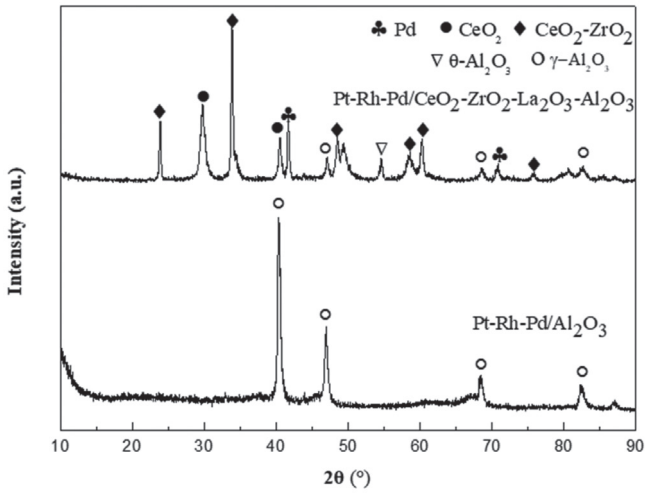

Figure 3. *XRD spectrums of Pt-Rh-Pd / Al_2O_3 catalyst and Pt-Rh-Pd / CeO_2-ZrO_2-La_2O_3-Al_2O_3 catalyst*

the formation of α-Al_2O_3, thereby maintaining the high dispersion of the active components and increasing the specific surface area of the catalyst.

Figure 4 shows the FT-IR spectra of Pt-Rh-Pd / CeO_2-ZrO_2-La_2O_3-Al_2O_3 fibrous catalyst after pre-oxidation at 80 °C (a) and carbonization at 1100 °C (b). As shown in Figure 4(a), typical absorption peaks that appear at 2920 cm^{-1} and 1466 cm^{-1} are mainly caused by the stretching vibration and bending vibration of the C-H bond in PVP. The absorption peak at 3357 cm^{-1} is attributed to H-OH stretching in PVP. The absorption peak at 1642 cm^{-1} is attributed to the C=C stretching vibration in PVP. The absorption peak at 1294 cm^{-1} is generated by the C-O stretching vibration in $C_6H_{14}O$. From Figure 4(b), it is found that when the catalysts experienced carbonizing at 1100 °C for 1 h, all of the absorption peaks presented above finally disappeared, mainly in respect that PVP and the solvent (C_2H_5OH, DMF) in the catalysts are thermally decomposed and volatilized during the heating process. It proves that Pt-Rh-Pd / CeO_2-ZrO_2-La_2O_3-Al_2O_3 fibrous catalyst is decomposed to generate stable carbon fiber structure and metal oxide structure after pre-oxidation and carbonization.

Figure 5 shows the EDS diagram of Pt-Rh-Pd / CeO_2-ZrO_2-La_2O_3-Al_2O_3 fibrous catalysts. It can be seen from the figure that a large amount of particles evenly distribute on the catalyst surface. In order to determine the composition of particles on the surface of the catalyst, the surface particles are analyzed applying EDS. From Figure 5, it is found that the content of Pd species in the particles is large, which proves that the Pd species can finely adhere to the surface of the fiber. Table 2 shows the element mapping of Pt-Rh-Pd / CeO_2-ZrO_2-La_2O_3-Al_2O_3 fibrous catalyst. As displayed in Table 2, the main components of the fiber are Al, Ce and Zr, while Pt, Rh and La are not detected, which may be attributed to the low content of Pt, Rh and La. It proves that Pt, Rh and La species are highly dispersed on the support materials.

The texture properties of Pt-Rh-Pd / CeO_2-ZrO_2-La_2O_3-Al_2O_3 fibrous catalyst are shown in Table 3. N_2 adsorption-desorption isotherms (a) and pore size distribution (b) of Pt-Rh-Pd / CeO_2-ZrO_2-La_2O_3-Al_2O_3

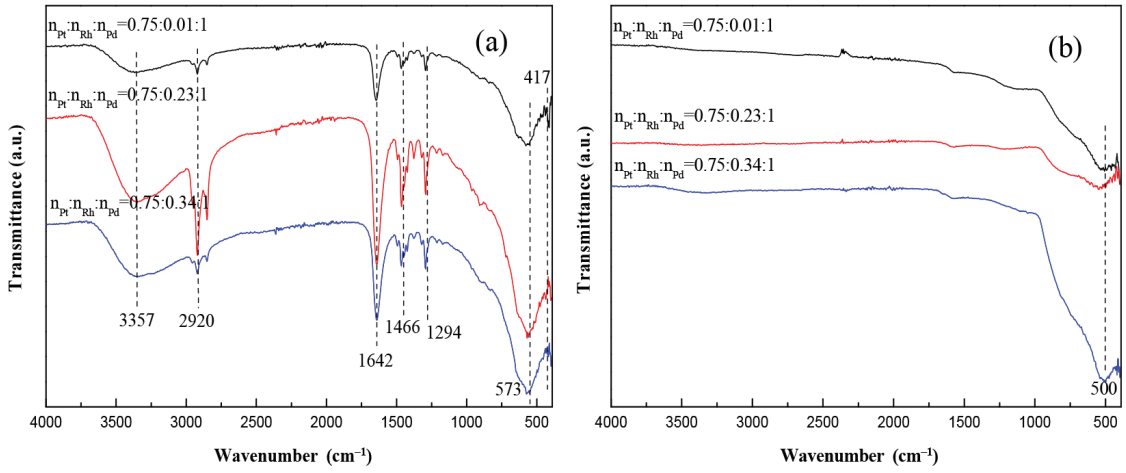

Figure 4. *FT-IR spectra of Pt-Rh-Pd / CeO_2-ZrO_2-La_2O_3-Al_2O_3 fibrous catalysts prepared at different molar ratios of Pt Rh and Pd after pre-oxidation at 80 °C (a) and carbonization at 1100 °C (b)*

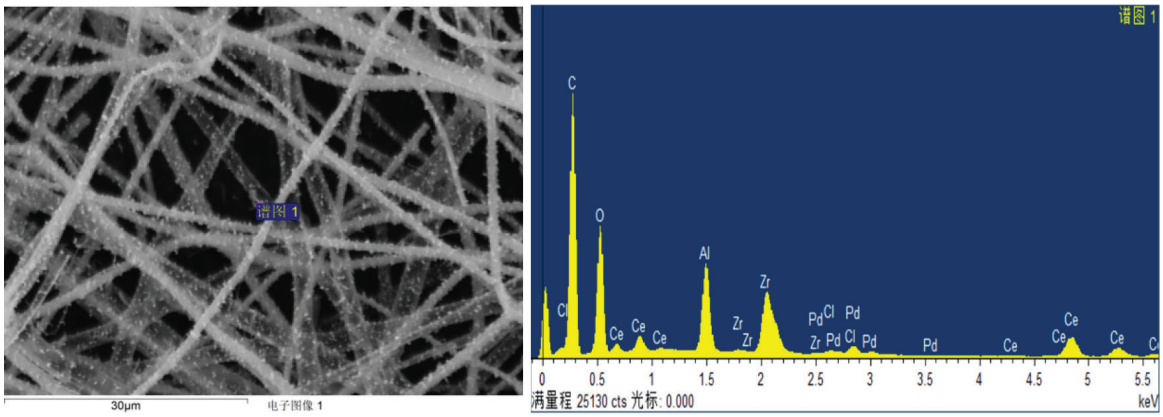

Figure 5. *EDS diagram of Pt-Rh-Pd / CeO_2-ZrO_2-La_2O_3-Al_2O_3 fibrous catalyst*

Table 2. Element mapping of Pt-Rh-Pd/ CeO_2-ZrO_2-La_2O_3-Al_2O_3 fibrous catalyst

Element	Weight percentage (%)	Atomic percentage (%)
C	42.07	61.84
O	28.11	31.01
Ce	12.08	1.52
Zr	10.78	2.09
Al	4.71	3.08
Pd	2.00	0.33
Cl	0.25	0.12

fibrous catalyst are shown in Figure 6. It is noticed from Table 1 that the pore diameter of the Pt-Rh-Pd / CeO_2-ZrO_2-La_2O_3-Al_2O_3 fibrous catalyst ranges from 2.42 nm to 4.68 nm, indicating that the fiber mainly belongs to the mesoporous material. The catalyst prepared with Pt Rh and Pd molar ratio of 0.75:0.01:1 has a maximum specific surface area of 301.5816 $m^2\ g^{-1}$. With the increase of Rh content, the specific surface area of the catalyst gradually decreases, while the pore diameter gradually increases. When the molar ratio of Pt Rh and Pd is 0.75:0.34:1, the pore diameter of the catalyst is 3.54 nm.

As displayed in Figure 6, the specific surface area of the Pt-Rh-Pd / CeO_2-ZrO_2-La_2O_3-Al_2O_3 fibrous catalyst decrease with the increase of Rh content, while the pore size of the catalyst gradually increases mainly due to the agglomeration between mesopores, which leads to the obvious increase of the pore size.

Surface morphology of Pt-Rh-Pd / CeO_2-ZrO_2-La_2O_3-Al_2O_3 fiber

Figure 7 shows the SEM images and diameter distribution histogram of Pt-Pd / CeO_2-ZrO_2-La_2O_3-Al_2O_3 fibrous catalyst. As displayed in Figures 7(a) and (b), the average diameter of the fiber filaments prepared with a $PtCl_4$ mass fraction of 0.35% is 800 nm. However, the electrospinning of inorganic metal oxide fibers is often accompanied by the solidification of the spinning solution at the needle, which causes the needle to become blocked and exacerbate the spinning instability. In addition, from Figures 7(c) and (d), the increase in the amount of Pt^{4+} strengthens the conductivity of the solution, which makes the fiber further stretched and refined by the electric field force. As seen in Figures 7(e) and (f), when the mass fraction of $PtCl_4$ increases to 0.65%, the fiber is greatly influenced by the electric field during the spinning process, which remarkably aggravates the spinning instability and leads to a large number of fiber fractures.

Figure 8 presents the SEM images and diameter distribution histograms of a Pt-Rh-Pd / CeO_2-ZrO_2-La_2O_3-Al_2O_3 catalysts. As seen therein, the fiber diameter of the Pt-Rh-Pd / CeO_2-ZrO_2-La_2O_3-Al_2O_3 catalyst is significantly larger than that of the Pt-Pd / CeO_2-ZrO_2-La_2O_3-Al_2O_3 catalyst. The average diameter of the fibers prepared with $RhCl_3$ mass fraction of 0.10% is 670 nm, which indicates that the Pt-Pd / CeO_2-ZrO_2-La_2O_3-Al_2O_3 catalyst has great surface morphology and uniform surface particle distribution. The average diameter of the fiber filaments increases to 710 nm when $RhCl_3$ mass fraction is 0.17%. From Figures 8(c) and (d), it is noticed that increasing $RhCl_3$ mass fraction will aggravate spinning instability and cause fiber breakage. As displayed in Figures 8(e) and (f), when the mass fraction of $RhCl_3$ increases to 0.25%, the average diameter of the filaments obviously increases to 790 nm with large agglomeration of particles on the fiber surface. $RhCl_3$ cannot be completely dissolved in the solvent and precipitates at the bottom of the precursor solution in the form of particles, which results in these particles directly attaching to the surface of the receiving plate during the spinning process.

Reduction performance of Pt-Rh-Pd / CeO_2-ZrO_2-La_2O_3-Al_2O_3 fibrous catalyst

The H_2-TPR spectrum of the Pt-Rh-Pd / CeO_2-ZrO_2-La_2O_3-Al_2O_3 fibrous catalyst is shown in Figure 9(a). As seen therein, Pt-Rh-Pd /

Table 3. Texture properties of catalysts prepared with different Rh contents

Samples		Specific surface area ($m^2\ g^{-1}$)	Pore volume ($cm^3\ g^{-1}$)	Pore diameter (nm)
Pt-Rh-Pd / Al_2O_3 catalyst	Pt Rh Pd molar ratio of 0.75:0.01:1	230	0.14	2.4
	Pt Rh Pd molar ratio of 0.75:0.23:1	149	0.10	2.5
	Pt Rh Pd molar ratio of 0.75:0.34:1	57	0.07	4.7
Pt-Rh-Pd / CeO_2-ZrO_2-La_2O_3-Al_2O_3 catalyst	Pt Rh Pd molar ratio of 0.75:0.01:1	302	0.18	2.4
	Pt Rh Pd molar ratio of 0.75:0.23:1	246	0.15	2.4
	Pt Rh Pd molar ratio of 0.75:0.34:1	199	0.18	3.5

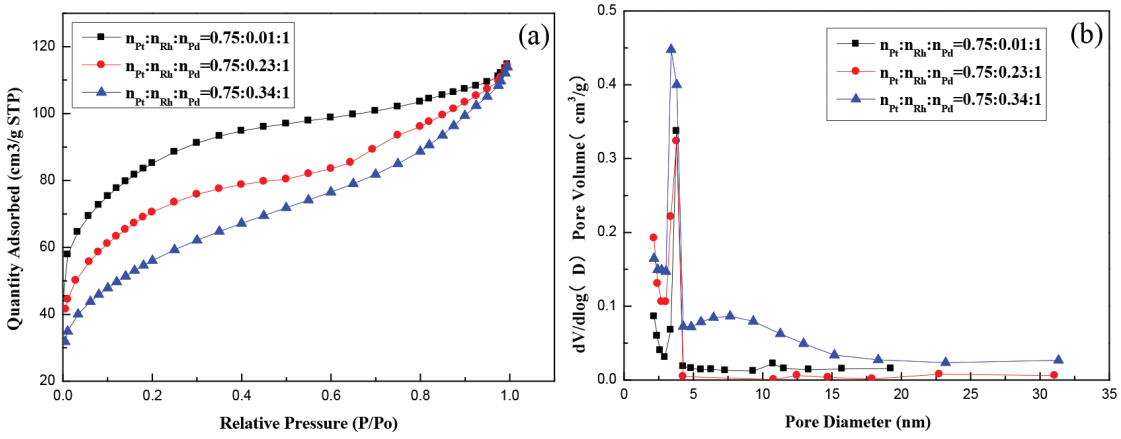

Figure 6. *N_2 adsorption-desorption isotherms (a) and pore size distribution (b) of Pt-Rh-Pd / CeO_2-ZrO_2-La_2O_3-Al_2O_3 fibrous catalysts*

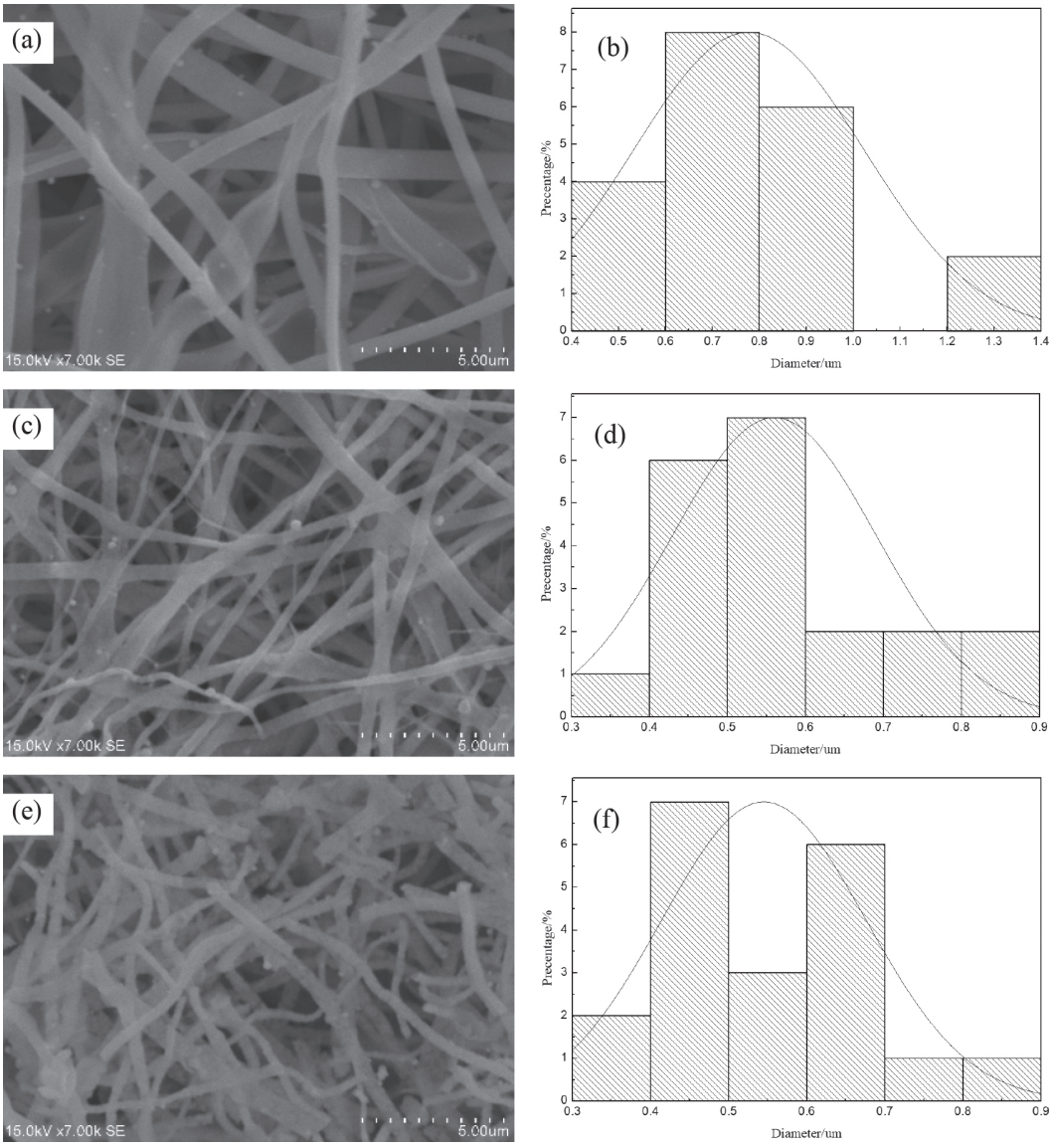

Figure 7. *SEM images and diameter distribution histograms of Pt-Pd / CeO_2-ZrO_2-La_2O_3-Al_2O_3 fibrous catalysts ((a) 0.35%$PtCl_4$, (c) 0.50%$PtCl_4$, (e) 0.65%$PtCl_4$)*

CeO_2-ZrO_2-La_2O_3-Al_2O_3 catalyst has three typical reduction peaks. The reduction peak is asymmetric and broad, indicating that various reducible species in fibrous catalyst are present. The addition of catalytically active components Pt, Rh and Pd move the reduction peak of the catalyst toward the low-temperature peak. The reduction peak at 220 °C for the catalyst is sharp, perhaps because Ce, Zr and La refine the size distribution of catalytic particles, which indicates that the catalyst has better low-temperature reduction performance. Compared with Pt-Rh-Pd / Al_2O_3 fibrous catalyst carrier from Figure 9(b) without the addition of Ce, Zr and La, the reduction rate has been greatly increased, reducing the reduction peak of the catalyst from 400 °C to 220 °C. In addition, the reduction peak area of the catalyst is large. Apparently, the catalytic particles formed on CeO_2-ZrO_2-La_2O_3-Al_2O_3 are stabilized by the support surface, indicating that Pt-Rh-Pd / CeO_2-ZrO_2-La_2O_3-Al_2O_3 catalyst has good thermal stability, which can maintain the original oxygen storage performance of the catalyst without being sintering at high temperatures.[18,21]

Pt-Rh-Pd / CeO_2-ZrO_2-La_2O_3-Al_2O_3 catalytic performance

Table 4 shows the catalytic performance of Pt-Rh-Pd / CeO_2-ZrO_2-La_2O_3-Al_2O_3 catalyst and Pt-Rh-Pd / Al_2O_3 catalyst. It can be obtained from Table 4 that the CO content in the vehicle exhaust without catalyst is 116 mg m^{-3} and the NO_X content is 14 mg m^{-3}. The tail gas contains 8 mg m^{-3} of SO_2, mainly due to the small amount of S contained in the 92 # gasoline used in the test vehicle. During the travel of the car, the SO_2 generated by the combustion of organic compounds containing S is emitted.

The self-assembled catalytic device where the content of Pd was 0.00056 mol and the molar ratio of Pt, Rh and Pd was 0.75:0.01:1 was installed on the car to analyze the components of the exhaust gas. It is found that the NO_X content after the installation of the catalyst is 1.4 mg m^{-3}. Adding Ce, Zr and La can effectively improve the catalytic performance of Pt-Rh-Pd / CeO_2-ZrO_2-La_2O_3-Al_2O_3 catalyst, and its catalytic efficiency for CO in automobile exhaust is 88.8%. The data shows that Ce, Zr and La can obviously improve the catalytic effect of Pt-Rh-Pd / CeO_2-ZrO_2-La_2O_3-Al_2O_3 catalyst, promote the oxygen storage performance of the catalyst and enhance the Pt-Rh-Pd / CeO_2-ZrO_2-La_2O_3-Al_2O_3 catalyst oxidative ability to CO.

CONCLUSIONS

Pt-Rh-Pd / CeO_2-ZrO_2-La_2O_3-Al_2O_3 fibrous catalyst for purifying automobile exhaust was prepared by electrospinning. The composition,

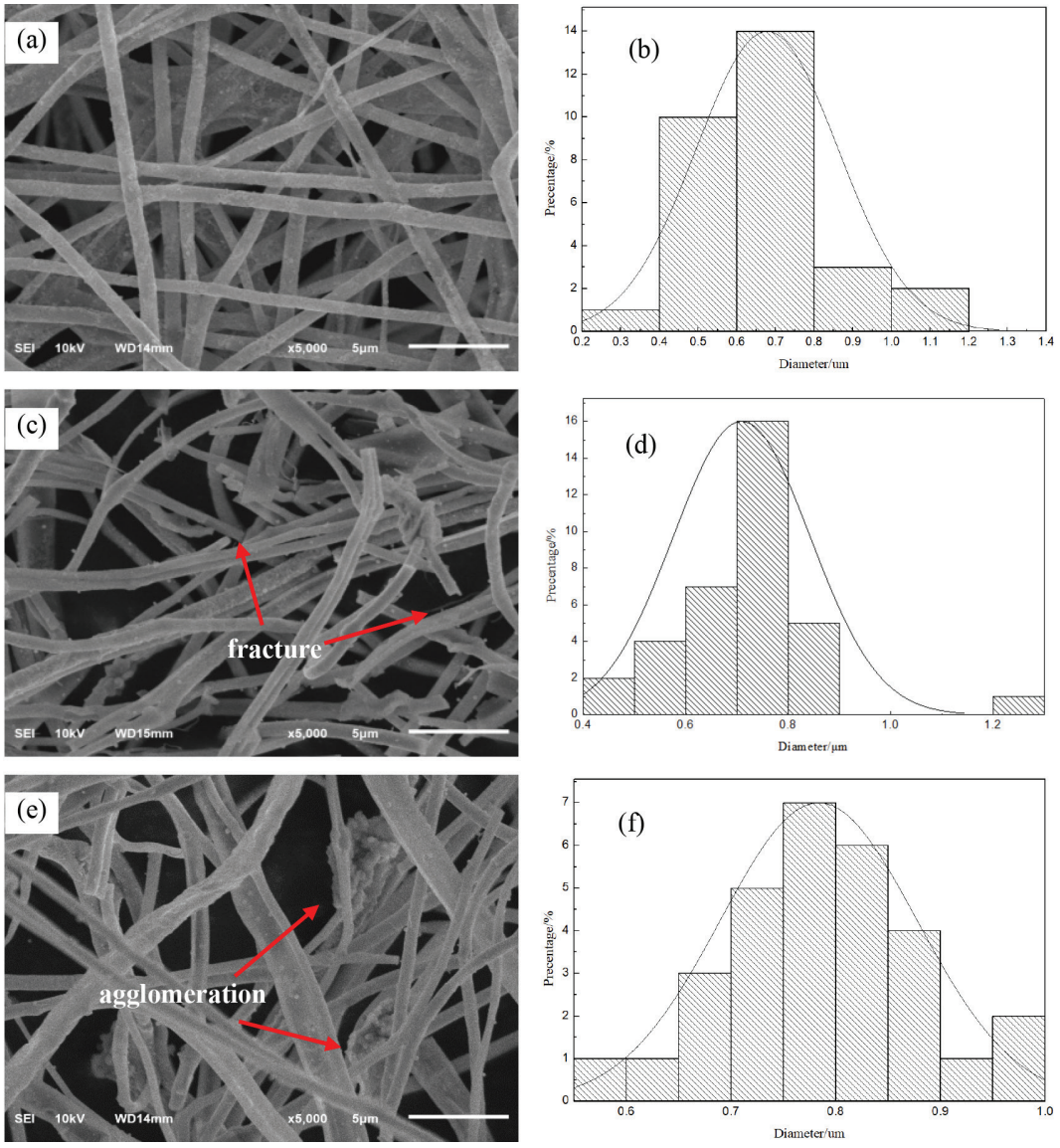

Figure 8. *SEM images and diameter distribution histograms of Pt-Rh-Pd / CeO_2-ZrO_2-La_2O_3-Al_2O_3 fibrous catalysts ((a) 0.10%$RhCl_3$, (c) 0.17% $RhCl_3$, (e) 0.25%$RhCl_3$)*

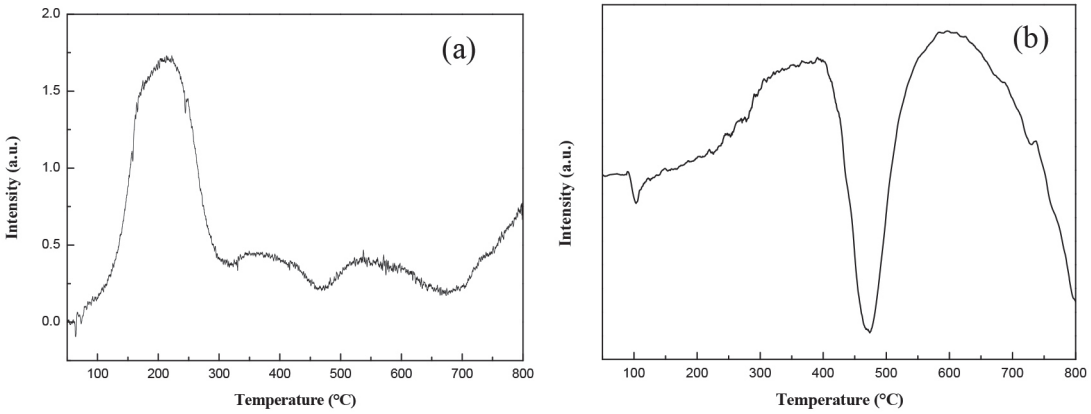

Figure 9. *H_2-TPR spectrum of Pt-Rh-Pd / CeO_2-ZrO_2-La_2O_3-Al_2O_3 fibrous catalyst (a) and Pt-Rh-Pd / Al_2O_3 fibrous catalyst (b)*

structure and surface morphology of the samples were studied by SEM-EDS, XRD FT-IR and BET analysis. In addition, the reduction performance of the catalyst was tested by H_2-TPR. The catalytic effect of catalyst on automobile exhaust was also investigated. From the experimental results, the following conclusions could be drawn:

- Pt-Rh-Pd / CeO_2-ZrO_2-La_2O_3-Al_2O_3 catalyst is mainly mesoporous, and Ce, Zr, La can effectively increase the specific surface area of Pt-Rh-Pd / CeO_2-ZrO_2-La_2O_3-Al_2O_3 catalyst. Meanwhile, the increase of Rh content will reduce the specific surface area of the catalyst and exacerbate the pore agglomeration on the

Table 4. Catalytic performance of Pt-Rh-Pd / CeO_2-ZrO_2-La_2O_3-Al_2O_3 catalyst and Pt-Rh-Pd / Al_2O_3 catalyst

Test items	catalytic performance of Pt-Rh-Pd / CeO_2-ZrO_2-La_2O_3-Al_2O_3 catalyst (%)	catalytic performance of Pt-Rh-Pd / Al_2O_3 catalyst (%)
NO_X	90.0	71.4
CO	88.8	54.3
SO_2	75.0	62.5
VOCS	68.1	47.9

catalyst surface, which causes the pore size of the catalyst to increase.

- The Pt-Rh-Pd / CeO_2-ZrO_2-La_2O_3-Al_2O_3 catalyst has a good surface morphology. Increasing the mass fraction of $RhCl_3$ will increase the fiber diameter and the spinning instability, resulting in fiber agglomeration and breakage.
- Ce, Zr and La can effectively improve the reduction ability of Pt-Rh-Pd / CeO_2-ZrO_2-La_2O_3-Al_2O_3 catalyst.

ACKNOWLEDGEMENTS

This work was supported by Jiangsu University Advantage Discipline Construction Project (Su Zheng Banfa [2018] No. 87), Jiangsu Province Key R&D Program (Industry Prospects and Common Key Technologies) (BE2018093) and Nantong Applied Research Program (JC2018115).

REFERENCES

1. Yan, X. G.; Hong, L.; Yu, X. H.; *Meteorol. Environ. Res*. **2015**, *6*, 30.
2. Larssen, S.; Nnesen. D. T.; Clench, A. J.; *Sci. Total Environ*. **1993**, *134*, 51.
3. Searles, R. A.; *Endeavour* **1989**, *13*, 2.
4. Miwa, K.; Kasai, H.; Padama, A. A.; *APS March Meeting - American Physical Society*, 2014.
5. Zheng, T.; Jun, J. H. E.; Zhao, Y.; *J. Rare Earths* **2014**, *32*, 97.
6. Shi, K. L.; Zhi, J. W.; Guo, Q. W.; Qing, S. Y.; Huan, Y. X.; *Hunan Nonferrous Metals* **2013**, *9*, 63.
7. Wang, J.; Chen, H.; Hu, Z.; *Catal. Rev*. **2015**, *57*, 79.
8. Deng, L.; Huang, C.; Kan, J.; Li, B.; Chen, Y.; Zhu, S.; *J. Rare Earths* **2018**, *36*, 49.
9. Lei, Z.; Xiang-ling, S.; Lei, Z.; Zhen-hua, M.; Hui-bin, H.; Xi, L.; *Nat., Environ. Pollut. Technol.* **2016**, *15*, 1071.
10. Suzuki, H.; Ota, K.; Saito, H.; *J. Eur. Ceram. Soc*. **1987**, *3*, 1.
11. Han, W.; Yi, H.; Tang, X.; *ChemistrySelect* **2019**, *4*, 4664.
12. Chen, M.; Wang, W.; Liang X.; *Adv. Energy Mater.* **2018**, *8*, 1800171.
13. Imtiaz, Q.; Kurlov, A.; Rupp, J. L. M.; *Ann. Chim. (Rome, Italy)* **2015**, *8*, 2055.
14. Jeamjumnunja, K.; Gong, W.; Makarenko, T.; Jacobson, A. J.; *J. Solid State Chem.* **2016**, *239*, 36.
15. Li, H. M.; Lan, L.; Chen, S. H.; *Acta Phys.-Chim. Sin.* (2016), doi: 10.3866/PKU.WHXB201603235.
16. Kondoh, H.; Hasegawa, N.; Yoshikawa, T.; Nakasaka, Y.; Tago, T.; Masuda, T.; *Energy Fuels* **2016**, *30*, 10358.
17. Liu, X.; Ning, P.; Xu, L.; *RSC Adv*. **2016**, *6*, 1800.
18. Jiang, H.; Wu, X.; Wang, C.; *Catal. Surv. Asia* **2017**, *21*, 37.
19. Guo, J.; Shi, Z.; Wu, D.; *Appl. Surf. Sci*. **2013**, *273*, 527.
20. Zhou, Y.; Deng, J.; Xiong, L.; *Mater. Des*. **2017**, *130*, 149.
21. Peng, N.; Zhou, J.; Chen, S.; *J. Rare Earths* **2012**, *30*, 342.
22. Byungchul, C.; Jongwoo, J.; Geonseog, S.; *Transaction of the Korean Society of Automotive Engineers* **2006**, *14*, 8.
23. Kim, M. S.; Khang, G.; Lee, H. B.; *Prog. Polym. Sci*. **2008**, *33*, 138.
24. Guo, D.-D.; Zhang, Z.-h.; Han, L.; Zhang, G.-h.; Fang, S.-m.; Yan, C.-m.; *Polym. Bull*. (2016), doi: 10.14028/j.cnki.1003-3726.2016.04.003.
25. Manea, L. R.; Cramariuc, B.; Popescu, V.; *Mater. Plast. (Bucharest, Rom.)* **2015**, *52*, 180.
26. Aysel, K. F.; Bilge, C. F.; *J. Colloid Interface Sci*. **2018**, *533*, 82.
27. Prasongthum, N.; Reubroycharoen, P.; *Key Eng. Mater*. **2015**, *659*, 221.